catalysts

MDPI

Article

Plasma Oxidation of H_2S over Non-stoichiometric La_xMnO_3 Perovskite Catalysts in a Dielectric Barrier Discharge Reactor

Kejie Xuan [1], Xinbo Zhu [1,2,3,*], Yuxiang Cai [2] and Xin Tu [3,*]

1 Faculty of Maritime and Transportation, Ningbo University, Ningbo 315211, China; xuankejie@sina.com
2 State Key Laboratory of Clean Energy Utilization, Zhejiang University, Hangzhou 310027, China; yxcai01@sina.com
3 Department of Electrical Engineering and Electronics, University of Liverpool, Liverpool L69 3GJ, UK
* Correspondence: zhuxinbo@nbu.edu.cn (X.Z.); xin.tu@liv.ac.uk (X.T.); Tel.: +86-574-8760-0505 (X.Z.); +44-151-794-4513 (X.T.)

Received: 12 July 2018; Accepted: 23 July 2018; Published: 2 August 2018

Abstract: In this work, plasma-catalytic removal of H_2S over La_xMnO_3 (x = 0.90, 0.95, 1, 1.05 and 1.10) has been studied in a coaxial dielectric barrier discharge (DBD) reactor. The non-stoichiometric effect of the La_xMnO_3 catalysts on the removal of H_2S and sulfur balance in the plasma-catalytic process has been investigated as a function of specific energy density (SED). The integration of the plasma with the La_xMnO_3 catalysts significantly enhanced the reaction performance compared to the process using plasma alone. The highest H_2S removal of 96.4% and sulfur balance of 90.5% were achieved over the $La_{0.90}MnO_3$ catalyst, while the major products included SO_2 and SO_3. The missing sulfur could be ascribed to the sulfur deposited on the catalyst surfaces. The non-stoichiometric La_xMnO_3 catalyst exhibited larger specific surface areas and smaller crystallite sizes compared to the $LaMnO_3$ catalyst. The non-stoichiometric effect changed their redox properties as the decreased La/Mn ratio favored the transformation of Mn^{3+} to Mn^{4+}, which contributed to the generation of oxygen vacancies on the catalyst surfaces. The XPS and H_2-TPR results confirmed that the Mn-rich catalysts showed the higher relative concentration of surface adsorbed oxygen (O_{ads}) and lower reduction temperature compared to $LaMnO_3$ catalyst. The reaction performance of the plasma-catalytic oxidation of H_2S is closely related to the relative concentration of O_{ads} formed on the catalyst surfaces and the reducibility of the catalysts.

Keywords: plasmas-catalysis; non-thermal plasmas; perovskite catalysts; nonstoichiometry; H_2S oxidation

1. Introduction

The emission of odors from various sources including wastewater treatment and municipal solid waste (MSW) treatment facilities have become a public concern due to their negative effect on air quality and human health, especially on sensitive or sick people [1]. As a result, air quality control in the waste treatment facilities is important to ensure a comfortable environment for the workers and local residents. Great efforts have been devoted to the research and development of odor abatement technologies including wet scrubbing, active carbon adsorption, incineration and biofiltration, etc. [2–4]. However, these technologies are not cost-effective when dealing with low concentrations of odors in high-volume waste gas streams. For example, biological treatment is not flexible for the variation of odor loadings and volume of waste gas streams [5].

Recently, non-thermal plasma (NTP) has been regarded as a promising alternative for deodorization due to its unique characteristics of fast reaction, compact system and adaptability

towards complex working conditions [6,7]. Typically, air plasma could generate electrons and various chemically reactive species, which could react with the odor molecules, leading to the purification of the odor-containing waste gas streams. Anderson et al. performed an on-site test of a pilot scale plasma reactor to purify a 138 $m^3 \cdot h^{-1}$ odor-containing waste gas stream with the main compositions of acetic acid, propanoic acid, trimethylamine and indole, etc. The average odor removal efficiency of 97% could be achieved at an input power of 140.8 W [8]. Kuwahara et al. developed a dielectric barrier discharge (DBD) reactor with a laminated film-electrode for odor control, while the complete removal of 100 ppm odor was achieved at a discharge power of 10 W and a flow rate of 5 $L \cdot min^{-1}$ [9]. Lu et al. reported the decomposition of ammonia and hydrogen sulfide with self-designed gliding arc plasma reactor, while a removal efficiency of 100% was achieved at the applied voltage of 11 kV and the velocity of 4.72 $m \cdot s^{-1}$ [10]. Some researcher also performed scale-up studies of plasma technologies in odor control [11]. Dobslaw et al. performed a 35-day-long scale-up test of plasma odor removal in two industrial sites in Germany, while the odor concentration was significantly reduced by 95.9–98.3% [12]. They also used the scale-up plasma units to enhance the performance of a biotrickling filter, the odor removal efficiency of using plasma alone reached up to 93.9% [13]. However, the relative low selectivity towards the desired final products in the NTP process remains the main challenge for the use of NTP-based technologies in environmental clean-up.

In the last three decades, the combination of non-thermal plasma and heterogeneous catalysis, known as "plasma-catalysis" has been demonstrated as a promising emerging process for the removal of low concentration gas pollutants including odors with reduced formation of by-products and enhanced process performance [14–17]. Although $LaMnO_3$ perovskite type catalysts have been used in thermal catalytic reactions due to their relatively low cost, comparable activity, and thermal stability [18–20], the use of these catalysts in plasma chemical reactions for environmental clean-up or the synthesis of fuels and chemicals has been very limited. Hueso et al. found that the combination of lanthanum based perovskite catalysts and a microwave discharge plasma enhanced the conversion of low concentration methane (3600 ppm) by around 30% compared to the plasma process in the absence of a catalyst at a same energy density of 10 $W \cdot m^{-2}$ [21,22]. Vandenbroucke et al. reported that the removal of trichloroethylene was increased by 13.9% when packing a $Pd/LaMnO_3$ catalyst into a negative DC corona discharge reactor at a specific energy density (SED) of 460 $J \cdot L^{-1}$ compared to the plasma reaction without a catalyst. They also found that the coupling of the plasma-catalyst coupling significantly reduced the formation of major by-product $CHCl_3$ [23]. It is well recognized that the substitution of A and B sites of the perovskite catalysts could result in a structural non-stoichiometry, which might generate excess oxygen species on the catalyst surfaces and consequently affect the reaction performance [24]. To the best of our knowledge, the use of perovskite catalysts in plasma-catalytic odor control has not been reported yet, while the knowledge about the underlying mechanisms of the non-stoichiometric effect of the perovskite catalyst on the plasma-catalytic oxidation processes are still missing.

In this work, hydrogen sulfide (H_2S) is chosen as a model pollutant since it accounts for over 90% of the total mass concentration in the odor emissions [25]. The non-stoichiometric effect of La_xMnO_3 catalysts on the plasma-catalytic removal of low concentration H_2S was investigated in a DBD plasma reactor in terms of the removal of H_2S and sulfur balance. The physicochemical properties of the catalysts were determined using various characterization techniques, including Brunauer-Emmett-Teller (BET) surface measurement, X-ray diffraction (XRD), X-ray photoelectron spectroscopy (XPS) and temperature programmed reduction of H_2 (H_2-TPR) to understand the structure-activity relationships between the La_xMnO_3 catalysts and the plasma-catalytic process and the role of these catalysts in the plasma-catalytic process.

2. Results and Discussions

2.1. Physicochemical Properties of the Catalysts

Table 1 show the results of N_2 adsorption-desorption experiments. The non-stoichiometric effect of the La_xMnO_3 catalysts enlarged the specific surface areas (S_{BET}) by 5.7% to 23.5% compared to that of the $LaMnO_3$ catalyst (12.3 $m^2 \cdot g^{-1}$), while the $La_{0.9}MnO_3$ catalyst had the highest S_{BET}. Figure 1 shows the XRD patterns of the La_xMnO_3 catalysts. The formation of the perovskite phase was observed in all the catalysts and no obvious segregated phases of La_2O_3 and MnO_x were found. The stoichiometric $LaMnO_3$ catalyst exhibited a typical cubic perovskite structure (JCPDS 75-0440) of $LaMnO_3$. The cubic structure of the La_xMnO_3 catalysts remained unchanged when the La doping amount was decreased, while the orthorhombic structure of $LaMnO_3$ (JCPDS 89-2470) was observed for the La-rich catalysts ($x > 1$). According to Table 1, the cell volume of the La_xMnO_3 catalysts increased with the increase of La/Mn molar ratio. The expansion of unit cell could be attributed to the transformation of Mn^{4+} into Mn^{3+} and the incorporation of La^{3+} into the perovskite lattice of La_xMnO_3 considering the larger ion radius of La^{3+} (1.06 Å) and Mn^{3+} (0.65 Å) compared to that of Mn^{4+} (0.54 Å). The characteristic diffraction peak of $LaMnO_3$ (1 2 1) located at around 32.6° was slightly shifted to a lower 2θ value for the La-rich catalysts, while this peak in the XRD pattern of the Mn-rich catalysts ($x < 1$) was shifted to a higher 2θ value [26]. The non-stoichiometric catalysts had a smaller crystallite size compared to the $LaMnO_3$ catalyst (16.1 nm), while the $La_{0.90}MnO_3$ catalyst had the smallest crystallite size of 15.4 nm.

Table 1. Physicochemical properties of La_xMnO_3 catalysts.

Sample	S_{BET} ($m^2 \cdot g^{-1}$)	[1] Crystalline Size (nm)	Cell Volume (Å^3)	$Mn^{4+}/(Mn^{3+} + Mn^{4+})$ (%)	$O_{ads}/(O_{ads} + O_{lat})$ (%)
$La_{0.90}MnO_3$	15.2	15.4	58.6	43.2	60.7
$La_{0.95}MnO_3$	13.0	15.8	58.7	42.2	59.9
$LaMnO_3$	12.6	16.1	58.9	41.5	58.1
$La_{1.05}MnO_3$	13.7	15.9	233.2	40.8	57.6
$La_{1.10}MnO_3$	14.6	15.7	234.4	38.2	56.6

[1] Calculated from the diffraction peak of La_xMnO_3 located at 2θ = 32.6°.

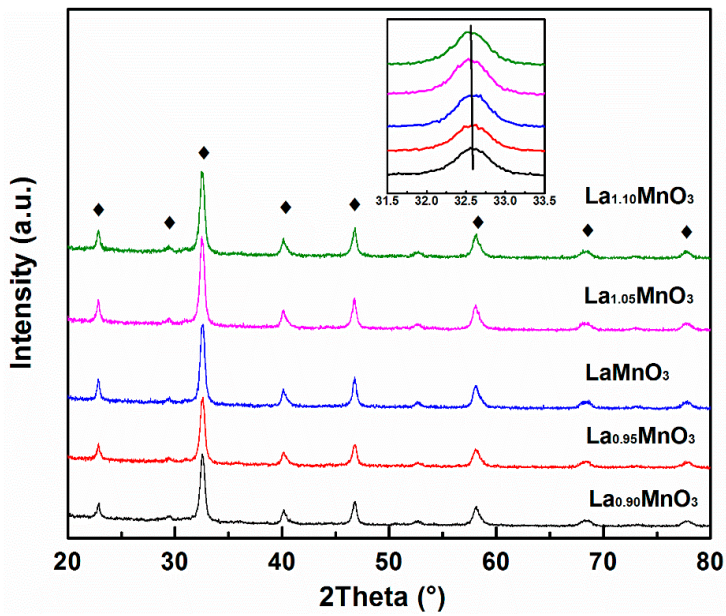

Figure 1. XRD patterns of La_xMnO_3 catalysts.

2.2. Redox Properties of the Catalysts

The chemical states of major elements (Mn 2p and O 1s) in the La_xMnO_3 catalysts were examined using XPS, as shown in Figure 2. The binding energies of La $3d_{5/2}$ (838.1 eV and 855.0 eV) were observed for all the catalysts (not shown), while those of La $3d_{3/2}$ were located at around 834.8 eV and 851.5 eV. The binding energies and the spin-orbit splitting of La 3d were close to those of pure La_2O_3, indicating that the lanthanum ions were in trivalent state of the La_xMnO_3 catalysts [27].

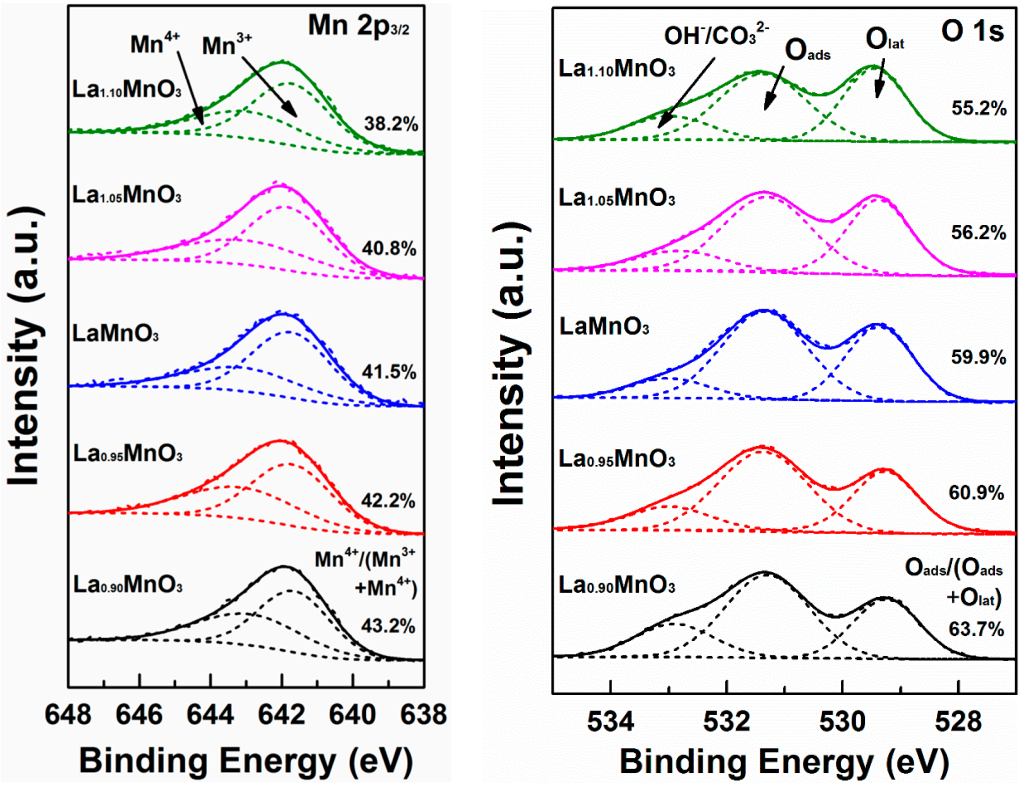

(**a**) (**b**)

Figure 2. XPS spectra of La_xMnO_3 catalysts: (**a**) Mn $2p_{3/2}$; and (**b**) O 1s.

Figure 2a shows the XPS spectra of Mn $2p_{3/2}$ of the La_xMnO_3 catalysts. The co-existence of Mn^{2+}, Mn^{3+} and Mn^{4+} species in the $LaMnO_3$-based perovskite catalysts has been reported [28]. However, in this work, Mn^{2+} species were unlikely existed due to the missing satellite peaks at around 648.8 eV [29]. The XPS signals of Mn $2p_{3/2}$ can be deconvoluted into two major peaks. The XPS peaks at 641.6 eV were assigned to the generation of Mn^{3+} cations, while the peaks at around 643.0 eV was associated to the formation of Mn^{4+} cations. The relative concentration of Mn^{4+} in the La_xMnO_3 catalysts, defined as $Mn^{4+}/(Mn^{3+}+Mn^{4+})$, was calculated based on the deconvoluted peaks (Table 1). The relative concentration of Mn^{4+} of these catalysts varied from 38.2% to 43.2%, and the $La_{0.90}MnO_3$ catalyst showed the highest value of 43.2%. The relative Mn^{4+} concentration of the catalysts decreased with the increase of nominal La/Mn molar ratio.

The deconvoluted O 1s spectra of the La_xMnO_3 perovskites suggested the coexistence of various oxygen species on the catalyst surface (Figure 2b). The peaks located at around 532.9 eV, 531.2 eV and 529.4 eV could be attributed to the formation of oxygen-containing groups: hydroxyl/carbonate species, surface adsorbed oxygen (O_{ads}) and lattice oxygen (O_{lat}), respectively [30]. The non-stoichiometric effect did not significantly change the binding energy of these three major oxygen species. Table 1 presents the relative concentration of O_{ads} of the catalysts, defined as $O_{ads}/(O_{ads} + O_{lat})$. The $La_{0.90}MnO_3$ catalyst showed the highest relative O_{ads} concentration of 60.7%, while the relative

concentration of O_{ads} of the catalysts decreased with the increase of nominal La/Mn molar ratio. Note that the variation of $O_{ads}/(O_{ads} + O_{lat})$ with the La/Mn molar ratio followed the same trend as $Mn^{4+}/(Mn^{3+} + Mn^{4+})$.

The reducibility of the La_xMnO_3 catalysts was analyzed using H_2-TPR experiment (Figure 3). For all the La_xMnO_3 catalysts, two major reduction peaks were observed. The first broad peak located between 200 °C and 500 °C could be divided into three sub-peaks. The shoulder peak centered between 200 °C and 300 °C could be ascribed to the reduction of weakly adsorbed oxygen species, while the second peak locate at around 350 °C was associated to the reduction of Mn^{4+} to Mn^{3+} with concomitant of surface adsorbed oxygen species. The third peak indicated the reduction of Mn^{3+} with coordination-unsaturated compose, while the peaks at higher temperature (above 600 °C) can be attributed to further reduction of Mn^{3+} to Mn^{2+} [27,31]. The lowest reduction temperature of the first broad peaks (335 °C and 392 °C) was observed over the $La_{0.90}MnO_3$ catalyst. Increasing the nominal La/Mn molar ratio slightly shifted the reduction peaks to higher temperatures. For example, the reduction temperatures of the $LaMnO_3$ catalyst were 342 °C and 393 °C, while those for $La_{1.10}MnO_3$ were 351 °C and 401 °C, respectively. This phenomenon indicated stronger interactions between La and Mn species, which inhibited the oxygen mobility on the La_xMnO_3 catalysts, and consequently decreased the reducibility of the catalysts.

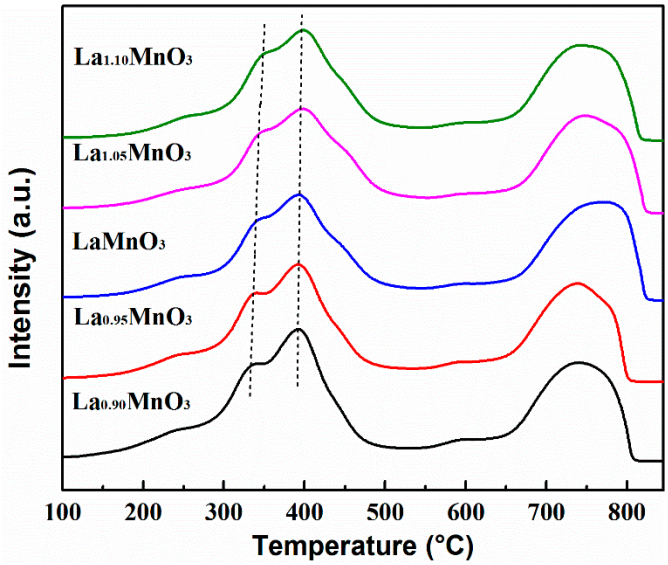

Figure 3. H_2-TPR profiles of La_xMnO_3 catalysts.

2.3. Plasma-Catalytic Oxidation of H_2S

The effect of the La_xMnO_3 catalysts on the removal of H_2S and the sulfur balance of the plasma-catalytic process was shown in Figure 4. The removal of H_2S increased monotonically with the increasing SED regardless of the presence of the catalysts. In the plasma reaction without a catalyst, the H_2S removal increased significantly from 10.7% to 41.5% when increasing the SED from 304.8 $J \cdot L^{-1}$ to 604.0 $J \cdot L^{-1}$, while the sulfur balance of the plasma process decreased from 98.2% to 74.3%. The input energy in a typical air plasma is mainly used to generate highly energetic electrons and chemically reactive species, including O, OH·, and nitrogen excited states $N_2(A)$, which contributed to the decomposition of the H_2S through direct electron-impact dissociation of H_2S and radical attack [6]. The dissociation of H_2S molecules by electrons with sufficient energy forms H· and SH· radicals [32], while the collision of H_2S with radicals (e.g., O and OH·) and excited nitrogen species also takes place in the plasma reaction [33]:

$$e + H_2S \rightarrow e + H\cdot + SH\cdot \quad (1)$$

$$N_2(A) + H_2S \rightarrow N_2 + H\cdot + SH\cdot \quad (2)$$

$$O + H_2S \rightarrow OH\cdot + SH\cdot \quad (3)$$

$$OH\cdot + H_2S \rightarrow SH\cdot + H_2O \quad (4)$$

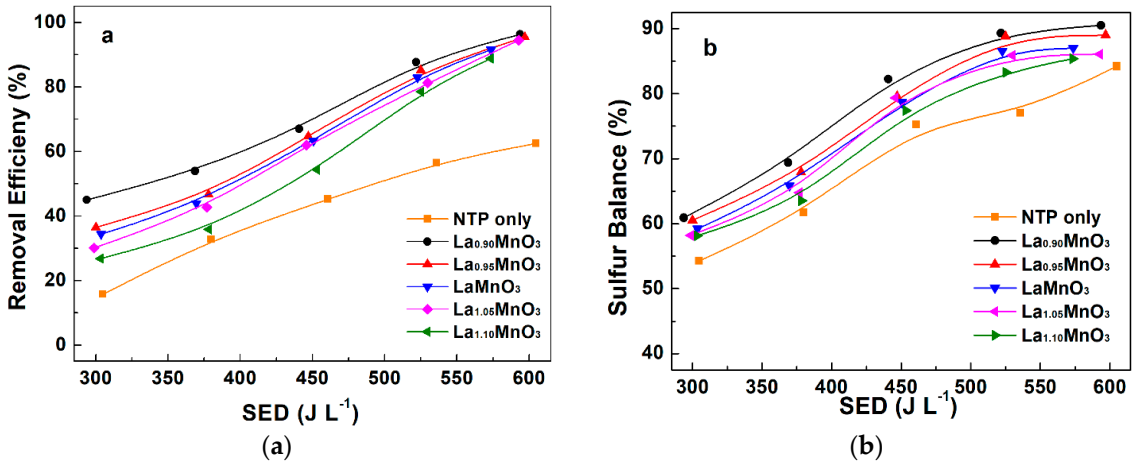

Figure 4. Effect of SED on plasma-catalytic removal of H_2S over La_xMnO_3 catalysts: (**a**) removal efficiency; and (**b**) sulfur balance of the plasma-catalytic process.

The generated H· radicals could be oxidized to form OH· by the oxidative species and participate the consequent plasma-induced reactions [6]. The SH· radicals were unstable in the oxidative environment and could be reacted with O and OH· radicals to form the major reaction product of SO_2:

$$SH\cdot + O\cdot \rightarrow SO\cdot + H\cdot \quad (5)$$

$$SH\cdot + OH\cdot \rightarrow SO\cdot + H\cdot \quad (6)$$

$$SO\cdot + O\cdot \rightarrow SO_2 \quad (7)$$

$$SO\cdot + OH\cdot \rightarrow SO_2 + H\cdot \quad (8)$$

The inner energy of the rotational and vibrational excited species, which were insufficient to break chemical bonds of H_2S molecules, could be transferred to the electronically excited species and accelerate the plasma-catalytic reactions [34]. NTP generated by the dielectric barrier discharge reactor consisted of numerous micro-discharges in the plasma region. The number of micro-discharges in each discharge period was increased at a higher SED with fixed gas flow rate, which creates more reaction channels for the decomposition of H_2S and intermediates, resulting in the enhanced removal of H_2S [35–37]. It is worth noting that no ozone was detected in this work, which might be consumed by local heating, catalytic effect, or plasma oxidation reactions [38]. The decreased sulfur balance at a higher SED can be ascribed to the formation of sulfur via: (1) electron impact dissociation of SH· radicals, and (2) disproportionation of SH· radical and recombination between SO_2 and H_2S [14]:

$$e + SH\cdot \rightarrow e + S + H\cdot \quad (9)$$

$$SH\cdot + SH\cdot \rightarrow S + H_2S \quad (10)$$

$$H_2S + SO_2 \rightarrow S + H_2O \quad (11)$$

The oxidation of SO_2 to SO_3 by highly oxidative species present in a plasma was reported by Jarrige et al. [39]:

$$SO2 + O\cdot \rightarrow SO3 \quad (12)$$

$$SO2 + OH\cdot \rightarrow SO3 + H\cdot \quad (13)$$

The presence of the La_xMnO_3 catalysts in the plasma region significantly enhanced the removal of H_2S and the sulfur balance compared to the plasma processing of H_2S without a catalyst. Figure 4 shows that the removal of H_2S increased from 34.3% to 91.6% in the plasma reaction over the stoichiometric $LaMnO_3$ when increasing the SED from 303.6 $J\cdot L^{-1}$ to 573.6 $J\cdot L^{-1}$, while the sulfur balance of the plasma-catalytic process increased from 59.2% to 87.0% under the same operating conditions. The increase of sulfur balance could be attributed to the enhanced oxidation of solid state sulfur to SO_2 at a higher SED, whilst the formation of a small amount of SO_3 was also observed. However, the formation of SO_3 in the plasma process was relatively low in this work (less than 8%), which was comparable to the results reported by Chang [40] and Kim et al. [41]. The non-stoichiometric effect of the La_xMnO_3 catalysts imposes a distinct effect on the plasma-catalytic removal of H_2S. Coupling the plasma with the $La_{0.90}MnO_3$ catalyst showed the highest H_2S removal of 96.4% and highest sulfur balance of 90.5% at a SED of 593.7 $J\cdot L^{-1}$. The increase of nominal La/Mn molar ratio inhibited the performance of the plasma-catalytic system for H_2S removal. The removal of H_2S and the sulfur balance follows the order of $La_{0.90}MnO_3$ > $La_{0.95}MnO_3$ > $LaMnO_3$ > $La_{1.05}MnO_3$ > $La_{1.10}MnO_3$ > NTP in the tested SED range, which is the opposite to the order of La/Mn molar ratio. Part of the missing sulfur element was found on the surface of the spent catalysts by XPS, which was also confirmed by a previous work [14].

Clearly, the La_xMnO_3 catalysts played a crucial role in the enhancement of the performance of the plasma-catalytic system. The non-stoichiometric effect slightly increased the specific surface area of the La_xMnO_3 catalysts by 3.2 to 20.6% compared to pure $LaMnO_3$ catalyst (12.6 $m^2\cdot g^{-1}$), while the crystalline size of the La_xMnO_3 catalysts was decreased by 0.9–9.8% (16.1 nm for the $LaMnO_3$ catalyst). The changes in the specific surface area and crystalline size of the catalysts indicated that the non-stoichiometric effect contributed to the strong interactions between the La and Mn species of the catalysts. Larger specific surface area could offer more adsorption sites and active sites in the plasma-catalytic reaction, which prolonged the residence time of H_2S and intermediates in the plasma reaction [42]. Previous study also confirmed that smaller crystallite sizes of the catalysts favored the exposures of active sites on the catalyst surface [43]. To sum up, the changes in the physicochemical properties of the La_xMnO_3 catalysts would increase the possibilities of effective collisions between the reactive species and the pollutant including H_2S and intermediates, which benefited the reaction performance of the plasma-catalysis system.

The XPS spectra confirmed the coexistence of Mn^{3+} and Mn^{4+} cations in the La_xMnO_3 catalysts. Charge imbalance may occur in the non-stoichiometric La_xMnO_3 regarding the change of the nominal La/Mn molar ratio in the perovskite structure [18,44]. Taking the $La_{0.90}MnO_3$ catalyst as an example, the decrease of La^{3+} content could form La vacancies in the perovskite lattice. The form of La vacancies could be compensated by the conversion of Mn^{3+} to Mn^{4+} to maintain the neutrality, which was evidenced by the production of highest relative concentration of Mn^{4+} of 43.2% in the $La_{0.90}MnO_3$ catalyst. Similar results were reported for the La-rich samples as more Mn^{3+} can be generated to maintain the electron neutrality in the presence of excess La cations [45]. The redox cycle between Mn^{3+} and Mn^{4+} was closely associated with the redox properties of the catalysts. The value of $Mn^{4+}/(Mn^{3+} + Mn^{4+})$ decreased from 43.2% to 38.2% when the La/Mn molar ratio increased from 0.90 to 1.10 in this work. The presence of Mn^{4+} species was also correlated with the formation of oxygen vacancies on the surface of the La_xMnO_3 catalysts [46]. Oxygen vacancies acted as the adsorption-desorption centers for the generation of O_{ads} from gas-phase oxygen species including O_2 molecules and O radicals in the plasma process. The oxygen species adsorbed on the oxygen vacancies (O_{ads}) played an important role in the plasma-induced surface reactions for the oxidation of H_2S and the intermediates due to the higher mobility of O_{ads} compared to the lattice oxygen (O_{lat}) [47]. Thus, perovskite catalysts with abundant oxygen vacancies were more active for the oxidation of pollutants on the catalyst surface in the plasma region. The $La_{0.90}MnO_3$ catalyst possessed the highest $O_{ads}/(O_{ads} + O_{lat})$ value of 60.7%, while increasing the nominal La/Mn molar ratio reduced the value

to 59.9% for $LaMnO_3$ and 55.2% for $La_{1.10}MnO_3$, respectively. Note the decrease of $O_{ads}/(O_{ads} + O_{lat})$ at higher La/Mn molar ratio was in line with the decreased $Mn^{4+}/(Mn^{3+} + Mn^{4+})$.

The reducibility of the La_xMnO_3 catalysts was also significantly affected by the non-stoichiometric effect. Figure 3 shows that the reduction temperatures of the Mn-rich catalysts were much lower compared to the La-rich catalysts and $LaMnO_3$, indicating that on the Mn-rich catalysts had a higher oxygen mobility. As mentioned before, the compensation effect of the insufficient or excess La species could promote or inhibit the formation of oxygen vacancies, which could contribute to the formation of surface adsorbed oxygen (O_{ads}) with higher oxygen mobility and consequently contributes to the enhanced oxidation of the adsorbed H_2S and intermediates to the final product of H_2O, SO_2, sulfur and possibly SO_3 in the plasma-catalytic system. It is noteworthy that the order of the reduction temperature of these catalysts was in consistent with the sequence of $O_{ads}/(O_{ads} + O_{lat})$ and $Mn^{4+}/(Mn^{3+} + Mn^{4+})$. Combining the results of XPS and H_2-TPR of these catalysts, it is clear that the redox properties of the catalysts play a determining role in the reaction performances of the plasma-catalytic removal of H_2S, while the non-stoichiometric effect at higher nominal La/Mn ratio inhibited the removal of H_2S in the plasma-catalytic system. The possible reaction mechanisms in the plasma-catalytic oxidation of H_2S over the La_xMnO_3 catalysts have been summarized in Figure 5.

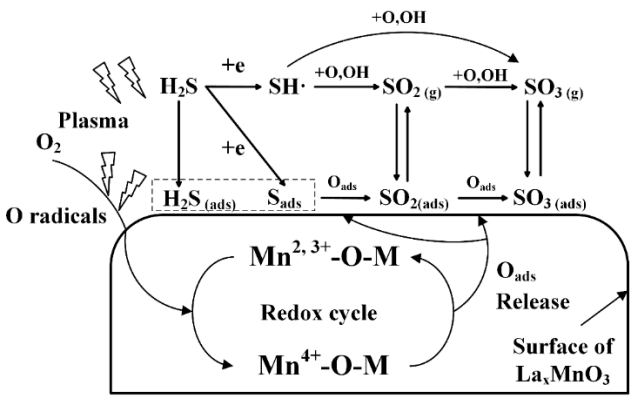

Figure 5. Reaction mechanisms of plasma-catalytic removal of H_2S over the La_xMnO_3 catalysts.

3. Experimental Setup

3.1. Catalyst Preparation

The non-stoichiometric La_xMnO_3 (x = 0.9, 0.95, 1, 1.05 and 1.1) perovskite-type catalysts were synthesized using a citric acid method, while lanthanum nitrate hexahydrate and 50 wt % manganese nitrate solution were used as the precursors [1]. All chemicals were analytic reagent and purchased from Aladdin Co. Ltd. (Shanghai, China) The synthesis procedures of the La_xMnO_3 catalysts were: (1) weighted amounts of all precursors and deionized water were mixed to obtain 0.1 M solutions; (2) a 50% excess amount of citric acid (comparing to the total amount of the metal cations) was added to the solution obtained in step 1 as the ligand; (3) the solution was thoroughly stirred for 3 h and evaporated in an 80 °C water bath to form viscous gel; (4) the gel was dried in an oven overnight at 110 °C and then calcined at 700 °C for 5 h; (5) the samples was then pressed and sieved to 35–60 meshes for testing.

3.2. Catalyst Characterizations

The specific surface area, average pore size and pore volume of the La_xMnO_3 catalysts were measured using N_2 adsorption-desorption experiments (Quantachrome Autosorb-1, Boynton Beach, FL, USA) at 77 K. The La_xMnO_3 catalyst samples were degassed at 200 °C for 5 h before each test. The specific surface area (S_{BET}) of the La_xMnO_3 catalyst was obtained by the Brunauer-Emmett-Teller (BET) equation.

The X-ray diffraction (XRD) measurements were carried out on a Rikagu D/max-2000 X-ray diffractometer (Tokyo, Japan) using Cu-Kα as the radiation source.

The X-ray photoelectron spectroscopy (XPS) experiments were performed with a Thermo ESCALAB 250 spectrometer (Waltham, MA, USA) using an Al Kα X-ray source (hν = 1486.6 eV). The XPS results were calibrated using the C 1s spectra at a binding energy (B.E.) of 284.6 eV.

The hydrogen temperature-programmed reduction (H_2-TPR) were performed using a Micrometrics Autochem II 2920 instrument (Ottawa, ON, Canada). For each test, 50 mg La_xMnO_3 catalyst samples were loaded and pretreated at 250 °C in a flowing N_2 for 1 h to remove the weakly adsorbed impurities and then cooled down to 50 °C. The samples were then heated from room temperature to 800 °C in a 5 vol % H_2/Ar flow (40 mL·min^{-1}). The heating rate was constant at 10 °C·min^{-1}. The H_2 consumption was calculated based on the H_2-TPR profiles.

3.3. Experimental Set-Up

The schematic experimental set-up is shown in Figure 6. The details of the DBD reactor were described elsewhere [26]. The reactor was co-axial type with the discharge length of 60 mm. The inner diameter of the discharge tube was 8 mm, while the outer diameter was 10 mm. The diameter of the stainless high voltage rod was 2 mm. Thus, the total plasma discharge volume was 2.26 mL. The carrier gas (high-purity air) and H_2S was generated from gas cylinders purchased from Jingong, Hangzhou, China. All gas streams were regulated by mass flow controllers and mixed prior to the plasma reactor. The total flow rate was 2 L·min^{-1}, while the initial H_2S concentration was 100 ppm. In this work, 100 mg La_xMnO_3 catalyst was used in each test. The catalysts was held in place by quartz wool, while only quartz wool was packed in the plasma region in the cases using plasma alone. The reactor was energized by an AC power supply (Suman CTP2000-K, Nanjing, China) and the discharge frequency was fixed at 10 kHz. The temperature at the outer wall of the reactor was measured using an infrared thermometer (Omega OS540, Norwalk, CT, USA). During the experiment process, it gradually increased to approximately 80 °C, while the outlet gas temperature was about 30 °C.

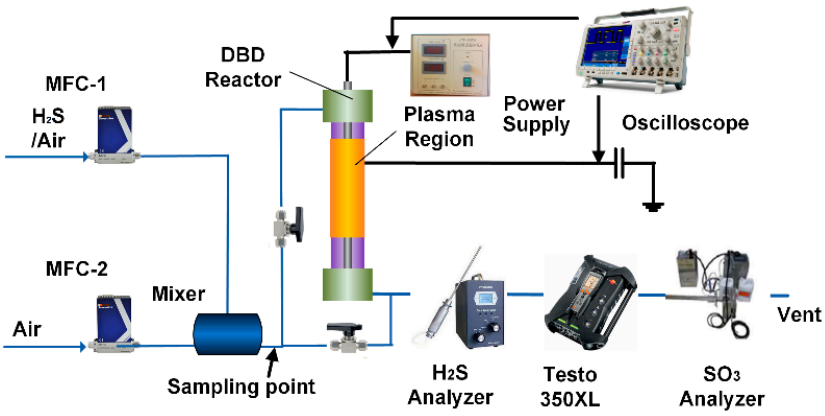

Figure 6. Schematic diagram of the experimental setup.

The applied voltage across the plasma-catalytic reactor was measured using a Tektronix 4034B digital oscilloscope connected to a Tektronix 6015A voltage probe (1000:1). An external capacitor was connected in series with the grounded electrode across which the voltage was measured using a TPP500 voltage probe (Tektronix, Beaverton, OR, USA). The average discharge power was calculated

by integrating the voltage waveforms by Q-U Lissajous method. The specific energy density (SED) of the plasma-catalysis process can be obtained as:

$$SED(\mathrm{J \cdot L^{-1}}) = \frac{P(\mathrm{W})}{Q\left(\mathrm{L \cdot min^{-1}}\right)} \times 60 \tag{14}$$

where P is the discharge power of plasma-catalytic process and Q is the total gas flow rate.

H_2S was measured by using a PTM-400 H_2S analyzer (Yiyuntian, Shenzhen, China) with the measuring range of 0–200 ppm and an accuracy of ±2%, while the concentration of formed SO_2 was measured by using a Testo 350XL gas analyzer (Lenzkirch, Germany) with an accuracy of ±5%. The concentration of outlet SO_3 was measured using a SO_3 analyzer (RJ-SO3-M) (Ruijing Tech., Shenzhen, China) based on the US EPA method 8 (specific IPA absorption method for SO_3 measurement). The detection range of the SO_3 analyzer was 0–200 ppm, while the average measuring error was less than 10% [48]. All data given in this work was the average value of three repeated measurements. The removal of H_2S (η_{H_2S}) and sulfur balance of the plasma-catalytic oxidation of H_2S can be defined as:

$$\eta_{H_2S}(\%) = \frac{c_{in} - c_{out}}{c_{in}} \times 100\% \tag{15}$$

$$Sulfur\ balance(\%) = \frac{c_{SO_2} + c_{SO_3}}{c_{in} - c_{out}} \times 100\% \tag{16}$$

where c_{in} and c_{out} are the H_2S concentration at the inlet and outlet of the reactor, respectively, while c_{SO_2} and c_{SO_3} are the outlet SO_2 and SO_3 concentrations.

4. Conclusions

A series of non-stoichiometric La_xMnO_3 catalysts were evaluated in the plasma-catalytic oxidative removal of H_2S using a non-thermal plasma DBD reactor in terms of H_2S removal and sulfur balance of the plasma process. The coupling of the DBD plasma with the La_xMnO_3 catalysts enhanced both H_2S removal and sulfur balance compared to the plasma process without using a catalyst. The highest H_2S removal of 96.4% was achieved at a SED of 593.7 $\mathrm{J \cdot L^{-1}}$ when placing the $La_{0.90}MnO_3$ catalyst in the DBD plasma reactor. In addition, the combination of the plasma with the $La_{0.90}MnO_3$ catalyst also showed the highest sulfur balance in the plasma-catalytic process. The non-stoichiometric effect of the La_xMnO_3 catalysts significantly affected the removal of H_2S since the reaction performance of the plasma-catalytic process decreased with the increasing nominal La/Mn molar ratio. Compared to pure $LaMnO_3$ catalyst, the non-stoichiometric La_xMnO_3 catalyst showed enhanced specific surface area and smaller crystallite size. The decreased La/Mn molar ratio in the La_xMnO_3 catalysts favored the transformation of Mn^{3+} cations to Mn^{4+}, which contributed to the formation of oxygen vacancies on the catalyst surfaces. The results of XPS and H_2-TPR demonstrated that the Mn-rich catalysts possessed higher relative concentration of surface adsorbed oxygen (O_{ads}) and better reducibility (lower reduction temperature) compared to pure $LaMnO_3$, which suggests that the relative concentration of O_{ads} and reducibility of the catalysts played a key role in determining the reaction performance of the plasma-catalytic removal of H_2S.

Author Contributions: Conceptualization: X.Z. and X.T.; data curation: K.X., X.Z., and Y.C.; formal analysis: Y.C.; investigation: K.X. and X.Z.; methodology: X.Z. and Y.C.; writing—original draft: X.Z.; writing—review and editing: X.Z. and X.T.

Funding: This research was funded by National Natural Science Foundation of China (no. 51606166) and K.C. Wong Magna Fund in Ningbo University, China.

Conflicts of Interest: The authors declare no conflict of interest.

References

1. Bogner, J.E.; Chanton, J.P.; Blake, D.; Abichou, T.; Powelson, D. Effectiveness of a florida landfill biocover for reduction of CH_4 and nmhc emissions. *Environ. Sci. Technol.* **2010**, *44*, 1197–1203. [CrossRef] [PubMed]
2. Burgess, J.E.; Parsons, S.A.; Stuetz, R.M. Developments in odour control and waste gas treatment biotechnology: A review. *Biotechnol. Adv.* **2001**, *19*, 35–63. [CrossRef]
3. Schlegelmilch, M.; Streese, J.; Stegmann, R. Odour management and treatment technologies: An overview. *Waste Manag.* **2005**, *25*, 928–939. [CrossRef] [PubMed]
4. Zhang, L.; De Schryver, P.; De Gusseme, B.; De Muynck, W.; Boon, N.; Verstraete, W. Chemical and biological technologies for hydrogen sulfide emission control in sewer systems: A review. *Water Res.* **2008**, *42*, 1–12. [CrossRef] [PubMed]
5. Chen, L.; Hoff, S.J. Mitigating odors from agricultural facilities: A review of literature concerning biofilters. *Appl. Eng. Agric.* **2009**, *25*, 751–766. [CrossRef]
6. Vandenbroucke, A.M.; Morent, R.; De Geyter, N.; Leys, C. Non-thermal plasmas for non-catalytic and catalytic VOC abatement. *J. Hazard. Mater.* **2011**, *195*, 30–54. [CrossRef] [PubMed]
7. Van Durme, J.; Dewulf, J.; Leys, C.; Van Langenhove, H. Combining non-thermal plasma with heterogeneous catalysis in waste gas treatment: A review. *Appl. Catal. B Environ.* **2008**, *78*, 324–333. [CrossRef]
8. Andersen, K.B.; Feilberg, A.; Beukes, J.A. Abating odour nuisance from pig production units by the use of a non-thermal plasma system. In Proceedings of the International conference on environmental odour monitoring and control (NOSE), Florence, Italy, 22–24 September 2010; pp. 351–356.
9. Kuwahara, T.; Okubo, M.; Kuroki, T.; Kametaka, H.; Yamamoto, T. Odor removal characteristics of a laminated film-electrode packed-bed nonthermal plasma reactor. *Sensors* **2011**, *11*, 5529–5542. [CrossRef] [PubMed]
10. Lu, S.Y.; Chen, L.; Huang, Q.X.; Yang, L.Q.; Du, C.M.; Li, X.D.; Yan, J.H. Decomposition of ammonia and hydrogen sulfide in simulated sludge drying waste gas by a novel non-thermal plasma. *Chemosphere* **2014**, *117*, 781–785. [CrossRef] [PubMed]
11. Andersen, K.B.; Feilberg, A.; Beukes, J.A. Use of non-thermal plasma and UV-light for removal of odour from sludge treatment. *Water Sci. Technol.* **2012**, *66*, 1656. [CrossRef] [PubMed]
12. Dobslaw, D.; Ortlinghaus, O.; Dobslaw, C. A combined process of non-thermal plasma and a low-cost mineral adsorber for VOC removal and odor abatement in emissions of organic waste treatment plants. *J. Environ. Chem. Eng.* **2018**, *6*, 2281–2289. [CrossRef]
13. Dobslaw, D.; Schulz, A.; Helbich, S.; Dobslaw, C.; Engesser, K.-H. VOC removal and odor abatement by a low-cost plasma enhanced biotrickling filter process. *J. Environ. Chem. Eng.* **2017**, *5*, 5501–5511. [CrossRef]
14. Maxime, G.; Amine, A.A.; Abdelkrim, B.; Dominique, W. Removal of gas-phase ammonia and hydrogen sulfide using photocatalysis, nonthermal plasma, and combined plasma and photocatalysis at pilot scale. *Environ. Sci. Pollut. Res.* **2014**, *21*, 13127–13137. [CrossRef] [PubMed]
15. Ragazzi, M.; Tosi, P.; Rada, E.C.; Torretta, V.; Schiavon, M. Effluents from MBT plants: Plasma techniques for the treatment of VOCs. *Waste Manag.* **2014**, *34*, 2400–2406. [CrossRef] [PubMed]
16. Ochiai, T.; Ichihashi, E.; Nishida, N.; Machida, T.; Uchida, Y.; Hayashi, Y.; Morito, Y.; Fujishima, A. Field performance test of an air-cleaner with photocatalysis-plasma synergistic reactors for practical and long-term use. *Molecules* **2014**, *19*, 17424–17434. [CrossRef] [PubMed]
17. Almarcha, D.; Almarcha, M.; Jimenez-Coloma, E.; Vidal, L.; Puigcercós, M.; Barrutiabengoa, I. Treatment efficiency by means of a nonthermal plasma combined with heterogeneous catalysis of odoriferous volatile organic compounds emissions from the thermal drying of landfill leachates. *J. Eng.* **2014**, *2014*, 831584. [CrossRef]
18. Dinh, M.T.N.; Giraudon, J.M.; Lamonier, J.F.; Vandenbroucke, A.; De Geyter, N.; Leys, C.; Morent, R. Plasma-catalysis of low tce concentration in air using $LaMnO_{3+\delta}$ as catalyst. *Appl. Catal. B Environ.* **2014**, *147*, 904–911. [CrossRef]
19. Nuns, N.; Beaurain, A.; Dinh, M.T.N.; Vandenbroucke, A.; De Geyter, N.; Morent, R.; Leys, C.; Giraudon, J.M.; Lamonier, J.F. A combined tof-sims and Xps study for the elucidation of the role of water in the performances of a post-plasma process using $LaMnO_{3+\delta}$ as catalyst in the total oxidation of trichloroethylene. *Appl. Surf. Sci.* **2014**, *320*, 154–160. [CrossRef]

20. Shi, C.; Zhang, Z.S.; Crocker, M.; Xu, L.; Wang, C.Y.; Au, C.T.; Zhu, A.M. Non-thermal plasma-assisted NO_x storage and reduction on a $LaMn_{0.9}Fe_{0.1}O_3$ perovskite catalyst. *Catal. Today* **2013**, *211*, 96–103. [CrossRef]
21. Hueso, J.; Cotrino, J.; Caballero, A.; Espinos, J.; Gonzalezelipe, A. Plasma catalysis with perovskite-type catalysts for the removal of NO and CH_4 from combustion exhausts. *J. Catal.* **2007**, *247*, 288–297. [CrossRef]
22. Hueso, J.L.; Caballero, A.; Cotrino, J.; González-Elipe, A.R. Plasma catalysis over lanthanum substituted perovskites. *Catal. Commun.* **2007**, *8*, 1739–1742. [CrossRef]
23. Vandenbroucke, A.M.; Nguyen Dinh, M.T.; Nuns, N.; Giraudon, J.M.; De Geyter, N.; Leys, C.; Lamonier, J.F.; Morent, R. Combination of non-thermal plasma and Pd/$LaMnO_3$ for dilute trichloroethylene abatement. *Chem. Eng. J.* **2016**, *283*, 668–675. [CrossRef]
24. Choi, J.J.; Billinge, S.J. Perovskites at the nanoscale: From fundamentals to applications. *Nanoscale* **2016**, *8*, 6206–6208. [CrossRef] [PubMed]
25. Kim, K.-H.; Choi, Y.J.; Jeon, E.C.; Sunwoo, Y. Characterization of malodorous sulfur compounds in landfill gas. *Atmos. Environ.* **2005**, *39*, 1103–1112. [CrossRef]
26. Zhu, X.; Gao, X.; Yu, X.; Zheng, C.; Tu, X. Catalyst screening for acetone removal in a single-stage plasma-catalysis system. *Catal. Today* **2015**, *256*, 108–114. [CrossRef]
27. Zhang, C.; Wang, C.; Zhan, W.; Guo, Y.; Guo, Y.; Lu, G.; Baylet, A.; Giroir-Fendler, A. Catalytic oxidation of vinyl chloride emission over $LaMnO_3$ and $LaB_{0.2}Mn_{0.8}O_3$ (B = Co, Ni, Fe) catalysts. *Appl. Catal. B Environ.* **2013**, *129*, 509–516. [CrossRef]
28. Zhu, X.; Liu, S.; Cai, Y.; Gao, X.; Zhou, J.; Zheng, C.; Tu, X. Post-plasma catalytic removal of methanol over Mn-Ce catalysts in an atmospheric dielectric barrier discharge. *Appl. Catal. B Environ.* **2016**, *183*, 124–132. [CrossRef]
29. Hou, Y.-C.; Ding, M.-W.; Liu, S.-K.; Wu, S.-K.; Lin, Y.-C. Ni-substituted $LaMnO_3$ perovskites for ethanol oxidation. *RSC Adv.* **2014**, *4*, 5329. [CrossRef]
30. Shen, M.Q.; Zhao, Z.; Chen, J.H.; Su, Y.G.; Wang, J.; Wang, X.Q. Effects of calcium substitute in $LaMnO_3$ perovskites for NO catalytic oxidation. *J. Rare Earth.* **2013**, *31*, 119–123. [CrossRef]
31. Quiroz, J.; Giraudon, J.-M.; Gervasini, A.; Dujardin, C.; Lancelot, C.; Trentesaux, M.; Lamonier, J.-F. Total oxidation of formaldehyde over MnO_x-CeO_2 catalysts: The effect of acid treatment. *ACS Catal.* **2015**, *5*, 2260–2269. [CrossRef]
32. Continetti, R.E.; Balko, B.A.; Lee, Y.T. Photodissociation of H_2S and the HS radical at 193.3 nm. *Chem. Phys. Lett.* **1991**, *182*, 400–405. [CrossRef]
33. Liang, W.-J.; Fang, H.-P.; Li, J.; Zheng, F.; Li, J.-X.; Jin, Y.-Q. Performance of non-thermal DBD plasma reactor during the removal of hydrogen sulfide. *J. Electrostat.* **2011**, *69*, 206–213. [CrossRef]
34. Aerts, R.; Martens, T.; Bogaerts, A. Influence of vibrational states on CO_2 splitting by dielectric barrier discharges. *J. Phys. Chem. C* **2012**, *116*, 23257–23273. [CrossRef]
35. Zheng, C.; Zhu, X.; Gao, X.; Liu, L.; Chang, Q.; Luo, Z.; Cen, K. Experimental study of acetone removal by packed-bed dielectric barrier discharge reactor. *J. Ind. Eng. Chem.* **2014**, *20*, 2761–2768. [CrossRef]
36. Aerts, R.; Tu, X.; De Bie, C.; Whitehead, J.C.; Bogaerts, A. An investigation into the dominant reactions for ethylene destruction in non-thermal atmospheric plasmas. *Plasma Process. Polym.* **2012**, *9*, 994–1000. [CrossRef]
37. Zhu, X.; Gao, X.; Qin, R.; Zeng, Y.; Qu, R.; Zheng, C.; Tu, X. Plasma-catalytic removal of formaldehyde over Cu-Ce catalysts in a dielectric barrier discharge reactor. *Appl. Catal. B Environ.* **2015**, *170–171*, 293–300. [CrossRef]
38. Holzer, F.; Kopinke, F.D.; Roland, U. Influence of ferroelectric materials and catalysts on the performance of non-thermal plasma (NTP) for the removal of air pollutants. *Plasma Chem. Plasma Process.* **2005**, *25*, 595–611. [CrossRef]
39. Jarrige, J.; Vervisch, P. Decomposition of gaseous sulfide compounds in air by pulsed corona discharge. *Plasma Chem. Plasma Process.* **2007**, *27*, 241–255. [CrossRef]
40. Chang, M.B.; Balbach, J.H.; Rood, M.J.; Kushner, M.J. Removal of SO_2 from gas streams using a dielectric barrier discharge and combined plasma photolysis. *J. Appl. Phys.* **1991**, *69*, 4409–4417. [CrossRef]
41. Hyun Ha, K.; Wu, C.; Takashima, K.; Mizuno, A. The influence of reaction conditions on SO_2 oxidation in a discharge plasma reactor. *IEEE Trans. Ind. Appl.* **1999**, *3*, 1478–1482.
42. Neyts, E.C. Plasma-surface interactions in plasma catalysis. *Plasma Chem. Plasma Process.* **2015**, *36*, 185–212. [CrossRef]

43. Tu, X.; Whitehead, J.C. Plasma-catalytic dry reforming of methane in an atmospheric dielectric barrier discharge: Understanding the synergistic effect at low temperature. *Appl. Catal. B Environ.* **2012**, *125*, 439–448. [CrossRef]
44. Hosseini, S.A.; Salari, D.; Niaei, A.; Oskoui, S.A. Physical-chemical property and activity evaluation of $LaB_{0.5}Co_{0.5}O_3$ (B = Cr, Mn, Cu) and $LaMn_xCo_{1-x}O3$ (x = 0.1, 0.25, 0.5) nano perovskites in VOC combustion. *J. Ind. Eng. Chem.* **2013**, *19*, 1903–1909. [CrossRef]
45. Chen, J.; Shen, M.; Wang, X.; Qi, G.; Wang, J.; Li, W. The influence of nonstoichiometry on $LaMnO_3$ perovskite for catalytic NO oxidation. *Appl. Catal. B Environ.* **2013**, *134–135*, 251–257. [CrossRef]
46. Dai, Y.; Wang, X.Y.; Li, D.; Dai, Q.G. Catalytic combustion of chlorobenzene over Mn-Ce-La-O mixed oxide catalysts. *J. Hazard. Mater.* **2011**, *188*, 132–139.
47. Zhang, Z.; Jiang, Z.; Shangguan, W. Low-temperature catalysis for VOCs removal in technology and application: A state-of-the-art review. *Catal. Today* **2016**, *264*, 270–278. [CrossRef]
48. Yang, Z.; Zheng, C.; Zhang, X.; Zhou, H.; Silva, A.A.; Liu, C.; Snyder, B.; Wang, Y.; Gao, X. Challenge of SO_3 removal by wet electrostatic precipitator under simulated flue gas with high SO_3 concentration. *Fuel* **2018**, *217*, 597–604. [CrossRef]